ELSEVIER

Journal of Structural Geology 29 (2007) 1201–1215

JOURNAL OF STRUCTURAL GEOLOGY

www.elsevier.com/locate/jsg

Fine-scale partitioning of contemporary strain in the southern Walker Lane: Implications for accommodating divergent strike-slip motion

Jonathan C. Lewis*

Department of Geoscience, 114 Walsh Hall, Indiana University of Pennsylvania, Indiana, PA 15705, USA

Received 28 June 2006; received in revised form 19 February 2007; accepted 20 February 2007
Available online 14 March 2007

Abstract

Treating the crust as a micropolar continuum and inverse modeling a high-quality catalog of earthquake focal mechanisms reveals that >km-scale heterogeneous strain is partitioned at ~km-scales into pairs of plane strains with sub-perpendicular principal axes. These earthquakes occurred in a shallow crustal volume centered on the western Indian Wells Valley of eastern California, the site of divergent, right-lateral strike-slip motion along the boundary between the Sierran microplate and the southern Basin and Range province. The seismic events defining the plane strains occur in a diffuse seismic source zone and cannot be additionally subdivided on the basis of the type of strain they accommodate. The results indicate that seismic moment release for background earthquakes is partitioned into events associated with either fault-zone-perpendicular extension by normal faults or horizontal shearing by conjugate strike-slip faults. The spatial scales over which this partitioning occurs suggest that outcrop-scale brittle faults may in some cases record nearly perpendicular plane strains related to a single continuous deformation.

Keywords: Walker Lane; Transtension; Seismogenic strain partitioning; Micropolar

1. Introduction

Geologists and geophysicists have long recognized that brittle deformation partitions spatially at many scales. Evidence comes from observations of thin-sections (Clark and Fisher, 1995), experimentally deformed analog models (Dooley and McClay, 1997; Tchalenko, 1968), outcrop-scale fault lineations (Cashman and Ellis, 1994), and plate-boundaries (Amelung and King, 1997; Cashman et al., 1992; Fitch, 1972; McCaffrey, 1992), to list but a few. This paper examines divergent strike-slip motion (i.e., transtension) along the southern Walker Lane belt of eastern California (Fig. 1). The primary goal is to highlight a linkage between contemporary deformation as constrained by geophysical data, and brittle faults preserved in the rock record. In particular, inverse modeling of earthquake focal mechanisms shows that background seismogenic strain is partitioned into pairs of plane strains with sub-perpendicular principal axes. These events define a diffuse seismic source zone within a single volume of crust and they cannot be further separated on the basis of the type of strain that they appear to accommodate. In spite of the fact that the events display a range of P axis (maximum instantaneous shortening) orientations, the modeled plane strains suggest that seismogenic deformation is partitioned to crustal thinning (normal faulting) and horizontal shearing (strike-slip faulting).

The results of this modeling elucidate the relatively early stages in the formation of a continental shear zone, and are relevant to understanding outcrop-scale brittle faults. First, small magnitude, background earthquakes reflect seismic flow (Kostrov, 1974), a process in which three-dimensional (3D) strain is accommodated by shearing on differently-oriented discrete slip surfaces (cf. Twiss and Unruh, 1998). The fact that 3D crustal strain is accommodated on networks of fault planes suggests that in some cases outcrop-scale brittle faults indeed reflect seismic

* Tel.: +1 724 357 5624; fax: +1 724 357 6208.
E-mail address: jclewis@iup.edu

0191-8141/$ - see front matter © 2007 Elsevier Ltd. All rights reserved.
doi:10.1016/j.jsg.2007.02.015

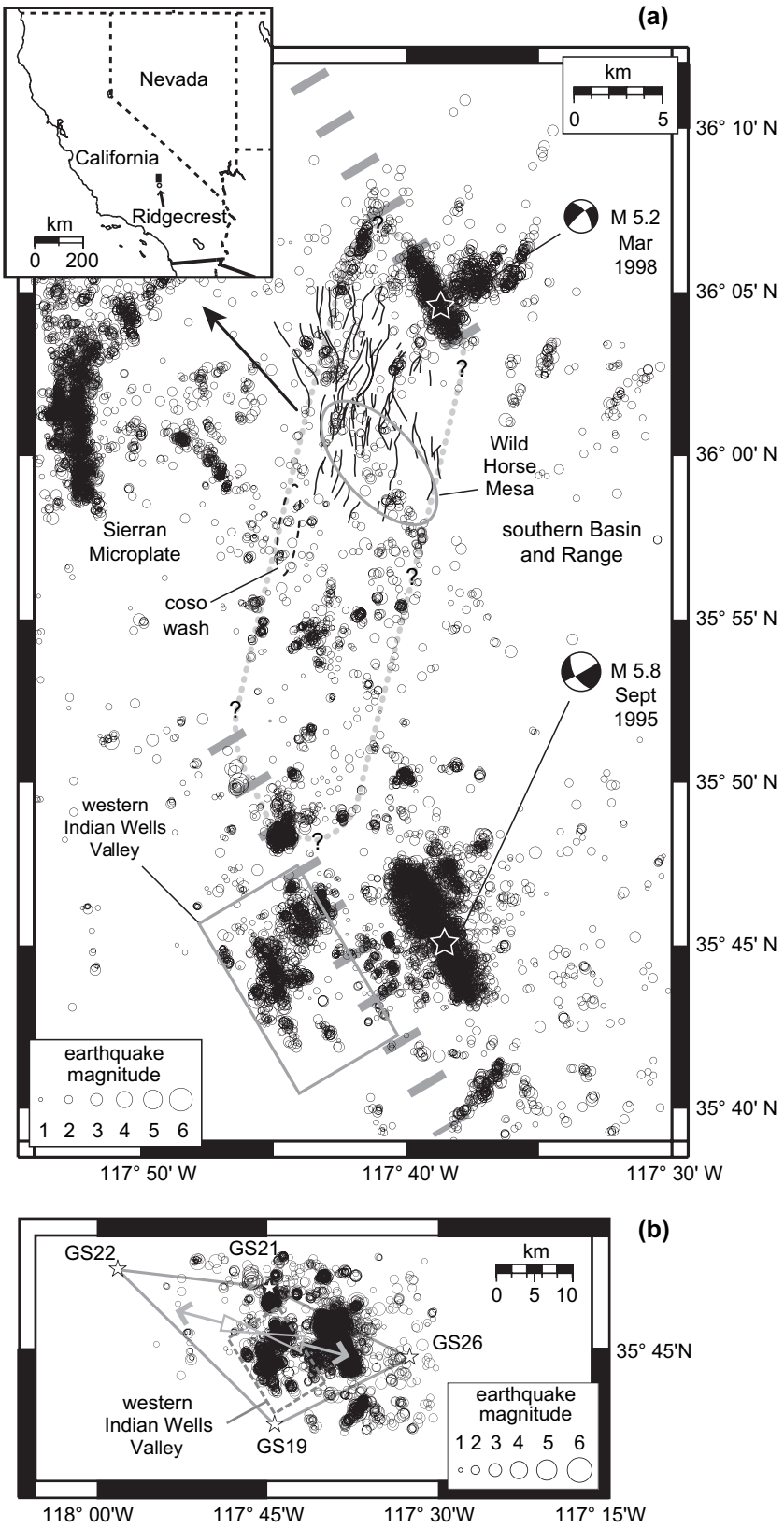

Fig. 1. (a) Mercator projection of the study area showing most of the major fault traces at Wild Horse Mesa (Duffield and Bacon, 1981), and earthquake locations (black circles and two white stars) in the region of the right-releasing stepover (light gray dotted outline) along the southeastern margin of the Sierran microplate (see also Hauksson et al., 1995; Unruh et al., 2002). The approximate boundary between the Sierran microplate and the southern Basin and Range province north and south of the stepover is shown by the wide dashed line segments. The area containing the 964 events in the western Indian Wells Valley is outlined with a gray box. (b) Mercator projection showing GPS stations, geodetically-derived contemporary maximum stretching direction (gray arrow with uncertainty at 1 sigma), and western Indian Wells Valley earthquake locations. Area spans from the southern Sierra Nevada mountains in the west (GS22) to the southern Argus Range in the east (GS26). The GPS velocities provided by S. McClusky and the GPS inversion program GPSTRN provided by R. Twiss.

flow, even in the absence of pseudotachylite (Cowen, 1999; Philpotts, 1964).

Second, the operation of a minimum of four slip systems is required to accommodate a 3D strain (e.g., Reches, 1978). In addition, it is apparent that the early development of this continental shear zone has been accommodated in the brittle crust by some combination of block rotation (Golombek and Brown, 1988; Pluhar et al., 2006; Schermer et al., 1996; Sonder et al., 1994), the development of shear fractures (Dewey, 2002; Lewis and Pluhar, 2003a), and/or the development of new slip directions on existing shear fractures (Carey-Gailhardis and Mercier, 1992; Lewis and Pluhar, 2003a). In a geologically young continental shear zone, such as the southern Walker Lane belt (Dixon et al., 1995; Dokka and Travis, 1990; Wernicke and Snow, 1998), block rotations and the development of new shear fractures may be an underlying control for the diffuse distribution of earthquakes (Lees, 2002; Unruh et al., 2002).

Third, the scale of rupture radii for background earthquakes is consistent with the mm- to cm-scale thicknesses of shear localization on many outcrop-scale faults (e.g., Lewis and Byrne, 2001; Peacock et al., 1998). Earthquakes with magnitudes between ~1.5–3 correspond, for example, to rupture radii on the order of tens to hundreds of meters. This scale of rupture radii is sufficient, however, to facilitate interactions and possible cross-cutting relations among differently-oriented faults within a volume of crust accommodating 3D strain by brittle failure. In total these simple observations highlight the potential of using high-quality earthquake focal mechanism solutions as a means of understanding exhumed brittle faults.

The results from the southern Walker Lane belt indicate that, for seismogenic deformation, heterogeneous, triaxial strain in the brittle crust may be partitioned as pairs of nearly orthogonal plane strains over ~km length scales. The approach entails inverting high-quality focal mechanism solutions (Hauksson, 2000) for partial strain-rate tensors that provide the best fit to the observed kinematics. To emphasize the fine scale of the partitioning that is apparent in the Indian Wells Valley, results from the nearby Wild Horse Mesa are also provided (Unruh et al., 2002).

2. Approach

A micropolar continuum model of crustal deformation (Twiss and Gefell, 1990; Twiss et al., 1991) is used as the basis for the inversion of seismic focal mechanism data to determine partial strain-rate tensors for the seismogenic component of non-recoverable shallow crustal deformation. This entails treating the crust essentially as a granular material that deforms by the movement of rigid blocks past one another along faults. The inverse problem assumes that slip on a seismogenic fault occurs in the direction of maximum shear rate on that surface, and that at the local scale the seismic P and T axes for a given earthquake are equivalent to the minimum and maximum instantaneous stretching directions, respectively (Twiss and Unruh, 1998). In this paper, distributed background seismic events ($M < 5$) are inverted for best-fitting partial strain-rate tensors. Because the inversion procedure can only provide the relative rather than absolute principal strain rates, the resulting tensors are referred to as *partial* strain-rate tensors. Experience using this approach to examine crustal deformation demonstrates that the resulting partial strain-rate tensors are in accord with independent geodetic and geologic observations of deformation (Lewis et al., 2003; Unruh and Lettis, 1998; Unruh and Twiss, 1998; Unruh et al., 1996; Twiss and Unruh, in press).

The application of micropolar continuum theory to the inverse problem yields five independent parameters that can be varied to provide a fit of the partial strain-rate tensor to focal-mechanism (or fault-slip) data (Twiss et al., 1993; Unruh et al., 1996). Three of the parameters are Euler angles that describe the orientations of the principal strain-rate axes (i.e., $d_1 \geq d_2 \geq d_3$; lengthening is reckoned positive). The deformation rate parameter:

$$D \equiv (d_2 - d_3)/(d_1 - d_3) \tag{1}$$

describes the relative magnitudes of the principal strain rates, and the relative vorticity parameter:

$$W \equiv (\omega_{13} - w_{13})/[0.5(d_1 - d_3)] \tag{2}$$

describes the normalized difference between the rotation rate of blocks (i.e., ω_{13}) and the large-scale continuum (i.e., w_{13}) about d_2. These five parameters are optimized using a down-hill simplex search algorithm (Press et al., 1989) that minimizes the average misfit between model slip directions and the slip directions inferred from the focal-mechanism data (or known from fault-slip data).

As noted above, slip on a fault is assumed to occur in the direction of the maximum rate-of-shear as defined by the micropolar continuum model (Twiss and Unruh, 1998). Given the geologically instantaneous nature of seismogenic deformation, it is equivalent to assume that slip occurs in the direction of maximum incremental shear strain.

The complete statistical assessment of each data subset includes the inversion of a minimum of 1000 bootstrap data sets (in some cases 2000 bootstrap data sets are analyzed). Each of these data sets is constructed by a process of random sampling of the actual data with replacement of the selected datum so that individual data points can be sampled (by chance) repeatedly. Random sampling with replacement continues until a bootstrap data set is constructed with a sample size equal to that of the actual data set. Inversion of 1000 (or more) bootstrap data sets provides a statistical basis for evaluating the robustness of the five model parameters determined for the full (actual) data set, including confidence limits on whether deformation is plane strain (i.e., $D = 0.5$) and/or whether crustal blocks are rotating at different rates than the large-scale continuum (i.e., $W \neq 0$).

This inverse method is akin to stress-based approaches that invert fault-slip or focal-mechanism data to find best-fitting partial stress tensors (Angelier, 1990; Gephart, 1990). Stress inversion methods, however, do not provide the degree of kinematic freedom necessary to account for block rotation, which geologic evidence suggests may be significant during some crustal deformation (Schermer et al., 1996;

Sonder et al., 1994; Wells, 1990; Wells and Coe, 1985). Comparisons of the value of *W* from micropolar inversion solutions with the surface geometry and kinematics of mapped fault blocks (Unruh et al., 1996), and with paleomagnetically determined rotations (Lewis and Pluhar, 2003a; Lewis and Pluhar, 2003b; Pluhar et al., 2006), show the inferred kinematics to be consistent, indicating that the parameter *W* measures a physically significant kinematic quantity.

3. Tectonic setting

Indian Wells Valley and Wild Horse Mesa are situated along the southeastern margin of the Sierran microplate (Fig. 1). Shearing here is less than ca. 3.9–0.7 Ma (Dixon et al., 1995; Dokka and Travis, 1990; Wernicke and Snow, 1998), and thus, background seismicity affords the opportunity to examine the early stages in the development of a through-going continental shear zone (Unruh et al., 2003). In this region the Sierran microplate moves toward the northwest at approximately 13–14 mm/yr relative to stable North America (Dixon et al., 2000). Seismogenic deformation within the Indian Wells Valley appears to be concentrated along the north northwest-trending Airport Lake fault zone (Roquemore, 1980), which accommodates ~50% of the total budget of contemporary Sierran-North America motion (McClusky et al., 2001). To the north, as this fault approaches the Coso Range, it appears to split into two branches. The west branch, referred to as the Little Lake fault, can be traced along the Sierra Nevada range front, and the east branch can be traced along the western margin of Coso Wash (Fig. 2; Unruh et al., 2002), through the area of Coso Hot Springs ultimately linking with the north-trending Haiwee Springs fault zone (Unruh et al., 2002). The latter fault has been estimated to have accommodated 5–6 km of right-lateral displacement (Walker and Whitmarsh, 1998).

Several observations suggest that contemporary deformation in the region is dominated by divergent strike-slip boundary conditions. Many of the mapped fault scarps and seismic source zones within this region trend more northerly than the trajectory of instantaneous motion of the Sierran microplate with respect to stable North America (Fig. 1a). Crustal extension is manifested by well-developed, west-facing normal fault scarps at Wild Horse Mesa (the ''step-faulted terrain'' of Duffield et al., 1980), immediately east of Coso Wash, and in seismogenic strain at shallow depths (discussed below and in Unruh et al., 2002). Horizontal displacement is evident in offset Mesozoic dike swarms cut by the Haiwee Springs fault (Walker and Whitmarsh, 1998) and in the seismogenic deformation below 5 km in the vicinity of Wild Horse Mesa (discussed below and in Unruh et al., 2002). In addition, paleomagnetic studies indicate that the normal fault blocks at Wild Horse Mesa record clockwise (looking down) vertical-axis rotations of ~12° (Pluhar et al., 2006). This finding coupled with field mapping and lava fingerprinting (Pluhar et al., 2005) suggest that the eastern margin of Wild Horse Mesa is the site of northwest-striking dextral shear (the Wild Horse Mesa fault of Pluhar et al., 2006). This structure is subparallel to a prominent northwest trending, 1998 earthquake swarm (Fig. 1).

In the Indian Wells Valley direct evidence for map scale structural geometry and kinematic behavior is poor because bedrock exposure is poor. A rhombic depression in the Indian Wells Valley west of the White Hills Anticline (see Fig. 2 for location) is suggestive of a small-scale right-releasing stepover (Roquemore, 1980). Right-slip is also indicated by the 1995 Ridgecrest earthquake sequence, which occurred in the eastern part of the Indian Wells Valley (Fig. 1 and Hauksson et al., 1995). In total the observations indicate that this region is dominated by large-scale dextral shearing with a component of crustal thinning (i.e., divergent right-lateral strike-slip boundary conditions).

Wild Horse Mesa lies largely south of the Coso Range (Fig. 2). The mesa is dominantly underlain by late Cenozoic basalt and andesite flows mostly less than ca. 3.7 Ma (Duffield and Bacon, 1981). Geochronologic results using $^{40}Ar/^{39}Ar$ indicate that these flows are 3.41 ± 0.04 Ma, and younger (Lewis and Pluhar, 2003a; Pluhar et al., 2005, 2006). North-striking normal fault scarps are well developed across the mesa and are associated with boundaries between relatively flat topographic benches that generally step down toward the west. The western edge of the mesa abuts Coso Wash, a broad alluvial fan that extends south toward the dry lakebed of Airport Lake, which lies north of the greater part of the Indian Wells Valley (Fig. 2).

Indian Wells Valley lies south of the late Cenozoic Coso volcanic field of the Coso Range (Fig. 1). The valley contains as much as 2 km of Miocene and Pliocene sediment deposited onto Mesozoic granitoid basement (see summary in Monastero et al., 2002). GPS geodesy indicates that the contemporary maximum stretching direction for crust straddling the Indian Wells Valley is oriented west northwest-east southeast (Fig. 1b). Seismicity within Indian Wells Valley displays a patchy distribution with two primary centers of activity (Fig. 1a). The first is a cluster of events that occurred between 1980–1997 in western Indian Wells Valley and the second is a cluster of events associated with the 1995 magnitude 5.4 Ridgecrest earthquake sequence in the eastern part of the valley (Hauksson et al., 1995).

In this paper results for 964 events from the 1980–1997 sequence in the western Indian Wells Valley (Hauksson, 2000), and subsets of these events, are presented. The extensive seismometer network and 3D crustal velocity model in this region of California ensure that the earthquake locations and focal mechanisms are of high quality. Histograms of misfit for these events show that 50% of the strike, dip and rake data fall within ranges of 10°, 18° and 15°, respectively (Unruh et al., 2002). The location errors for these events are at worst ~1 km horizontal and ~2 km vertical with the majority actually being much smaller, 50% or less of these values (Hauksson, 2000).

4. Seismogenic strain

4.1. Analyses and results – Wild Horse Mesa

Seismogenic deformation in the vicinity of Wild Horse Mesa varies with depth (Unruh et al., 2002) and is consistent with our understanding of divergent strike slip as revealed

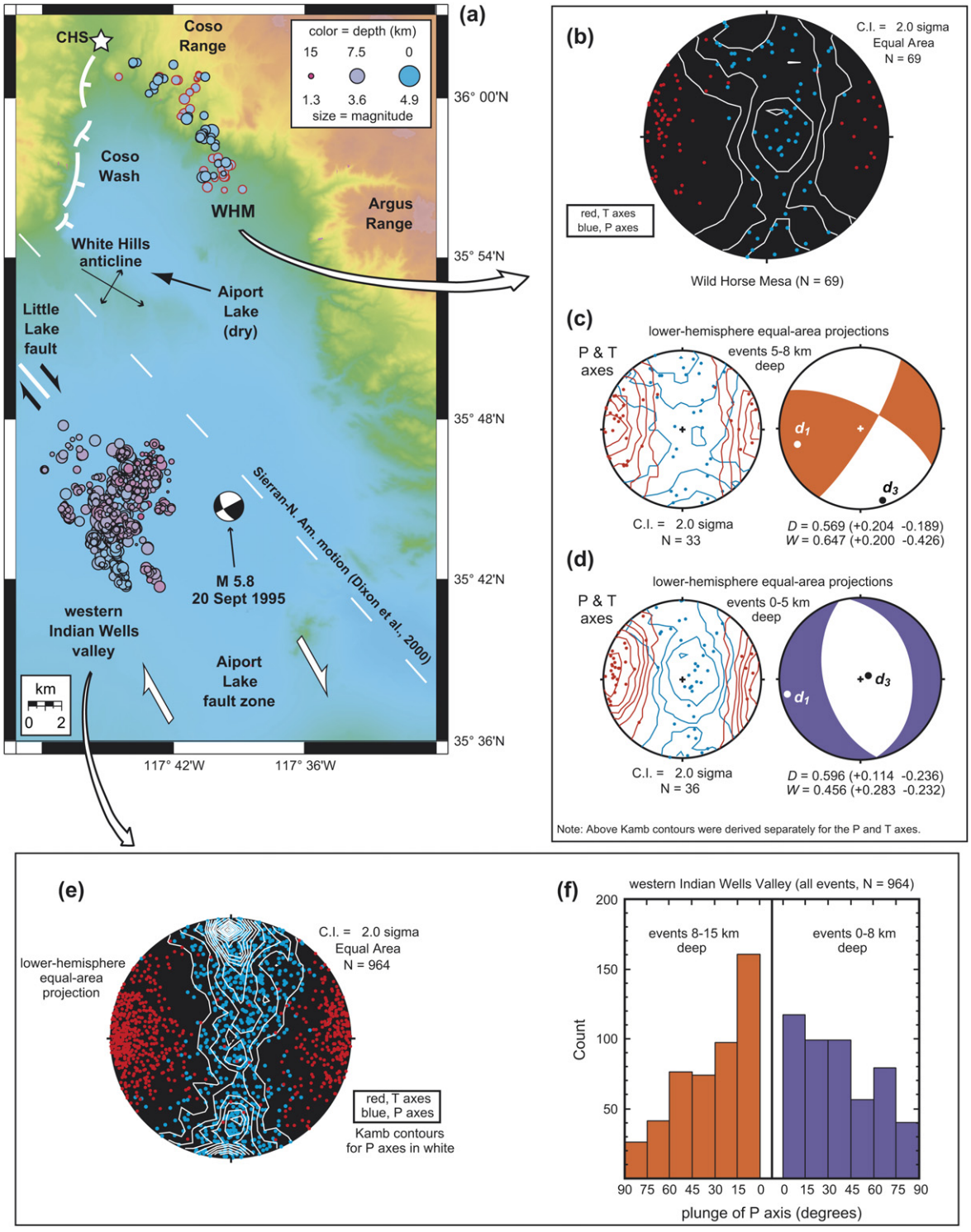

Fig. 2. (a) Mercator projection of part of the Coso Basin showing the locations of the seismic events from Wild Horse Mesa (WHM) and western Indian Wells Valley. See Tectonic Setting section for details of earthquake locations. Lower elevations are shown in cooler colors (≤1000 m), higher elevations in warmer colors (≥1400 m). WHM hypocenters in red are 5–8 km deep and those in black are 0–5 km deep. White lines show the approximate locations of the Little Lake fault and the Coso Wash normal fault (barbs on the downthrown side) from Unruh et al. (2002). CHS = Coso Hot Springs, area indicated with the white star. (b)–(d) Wild Horse Mesa plots as follows: (b) Seismic P and T axes in red and blue, respectively. (c) Seismic P and T axes (left) and partial strain-rate tensor (right), both for the deeper seismic events. (d) The same information is shown as in (c) but for the shallower seismic events. (e)–(f) Western Indian Wells Valley plots as follows: (e) Seismic P and T axes in red and blue, respectively. (f) Histogram of the plunge angle of the seismic P axes for deep (purple) and shallow (orange) seismic events.

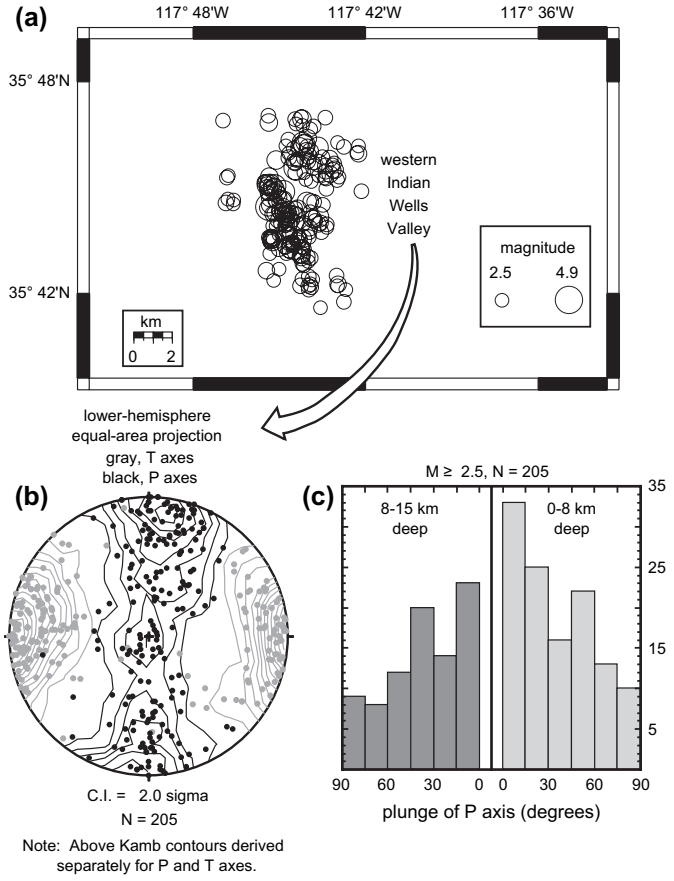

Fig. 3. (a) Mercator projection showing the locations of the 205 seismic events from the western Indian Wells Valley used to invert for partial strain-rate tensors. (b) Seismic P axes (black) and seismic T axes (gray) for these events. (c) Histogram of P axis plunge for these seismic events above and below 8 km. See text for discussion.

through analog models (Dooley and McClay, 1997; Dooley et al., 2003). Thirty six well-located seismic events (see previous section) from 0 to 5 km display a diffuse spatial distribution, whereas 33 well-located events from 5 to 8 km define a north northwest striking, steep, planar seismic source zone (Unruh et al., 2002). The seismic T axes (maximum instantaneous stretching directions) for all of these events are dominantly shallowly east or west plunging. In contrast the P axes (maximum instantaneous shortening directions) display a weakly bimodal distribution with both shallow north or south plunges, or subvertical orientations (Fig. 2b).

The best-fitting partial strain-rate tensors for these two depth-based subsets (Fig. 2c,d, right side) are distinct and suggest near surface crustal thinning (i.e., normal faulting) and deeper horizontal shearing (i.e., strike-slip faulting). For both subsets, results from 2000 bootstrap data sets show that D is statistically indistinguishable from 0.5, indicating plane strain, and that W is non-zero, indicating block rotations at rates different from the vorticity of the large-scale continuum deformation.

4.2. Analyses and results – western Indian Wells Valley

Seismogenic deformation in the western Indian Wells Valley displays similarities with, and important differences from the seismogenic deformation at Wild Horse Mesa. The seismic events occur in a somewhat heterogeneous distribution within a nominally cubic volume of crust ~11 km on a side (see Fig. 2a). As in the case of Wild Horse Mesa, the seismic T axes are well organized forming a prominent subhorizontal east-west maximum (Fig. 2e). The seismic P axes display a range of plunges much like that for Wild Horse Mesa with the exception that subhorizontal axes are dominant (Fig. 2e). The variation in plunge for P axes, however, is different than for Wild Horse Mesa in that for events both shallower and deeper than the mean event depth of 8 km, shallow plunges are considerably more common than steep plunges. Perhaps more significant is the observation that steep plunges, while not dominant, do occur in large numbers regardless of depth (note the weak girdle of P axis in Fig. 2e,f).

4.2.1. $M \geq 2.5$ events

A subset of larger magnitude seismic events was selected from the western Indian Wells Valley for detailed analyses. To maximize seismic station coverage, and thus data quality, a minimum magnitude cutoff of 2.5 was used and this reduced the sample size from 964 to 205 events. The orientations of

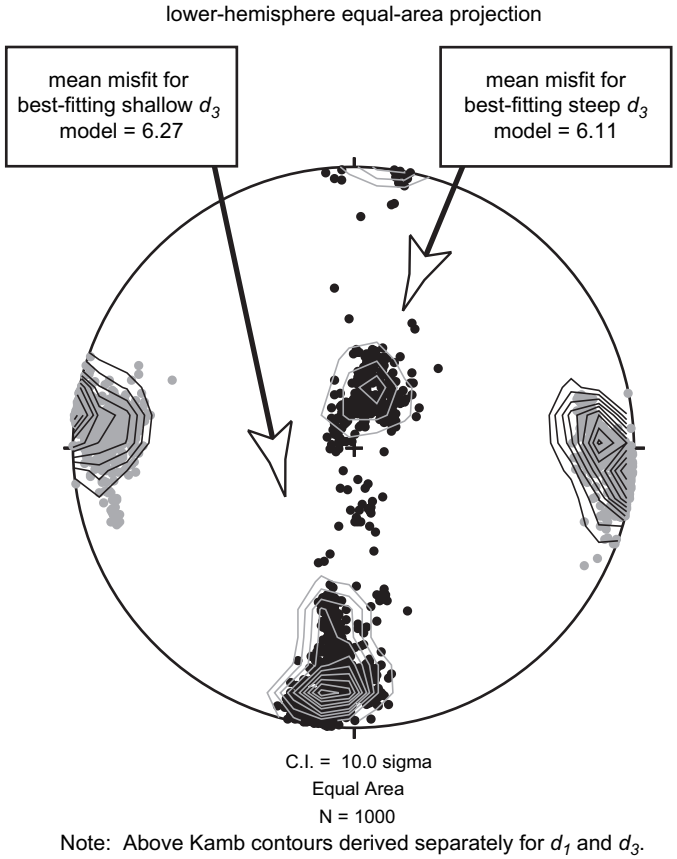

Fig. 4. Final positions for d_1 (light gray) and d_3 (black) axes for 1000 bootstrap data sets constructed for the 205 seismic events from the western Indian Wells Valley. The misfit values describe the mean angular deviations between the slip direction on model nodal planes and the slip direction indicated by the focal mechanisms.

seismic P and T axes, and the distribution of P axis plunges indicate that the subset of events is representative of the full data set (compare Fig. 3b with Fig. 2e).

Inverting 1000 bootstrap data sets in search of a single best-fitting partial strain-rate tensor provided a test of the homogeneity of the 205-event data set. The results (Fig. 4) indicate that a single solution is not possible, but rather that there are two distinct solutions that have comparable values of misfit, and that are characterized by differences in the orientation of the minimum stretching direction (d_3). The bootstrap results reveal final d_3 maxima that are either subvertical or shallowly south plunging, and that the proportion of models within these two maxima is comparable to the relative number of P axes with shallow versus steep plunges in the input data (compare Figs. 3b and 4). This result suggests that the 205 events constitute a mixed data set reflecting heterogeneous deformation at the scale of the crust in which the events occurred. Moreover, unlike at Wild Horse Mesa (see Fig. 2b–e), subdividing the seismic events on the basis of depth does not yield subsets for which single solutions are satisfactory (Figs. 2f and 3c). Subdivision of the western Indian Wells Valley data subset using other spatial binning schemes likewise failed to produce subsets that could be modeled with single solutions.

4.2.2. Strain-affinity subsets

The two point-maxima of d_3 positions for the 1000 bootstrap data sets generated for the 205, $M \geq 2.5$ events (Fig. 4) were used as a basis for subdividing the events into homogeneous subsets. For convenience, this approach is described here in the context of the results in Fig. 4, however, the same approach was used for additional data subsets described below. The two best-fitting (i.e., lowest misfit) partial strain-rate tensors for the two d_3 maxima in Fig. 4 were used as initial models with which all 205 of the focal mechanisms were evaluated. These two solutions consisted of the numerical best-fit values for the five micropolar model parameters (D, W, and the Euler angles for d_1, d_2 and d_3). These values define a partial strain-rate tensor for which the slip directions on model nodal planes were determined and compared with parallel focal mechanism nodal planes (i.e., data nodal planes). The angular disparity between the model slip directions and the slip directions inferred for the focal mechanisms was then used to: (1) determine which data nodal plane was better accounted for by the initial models; and (2) which model did a better job accounting for the kinematics of each datum. In this manner each datum was initially assigned to a subpopulation on the basis of the lowest misfit value for the two initial models (see "preliminary affinity" boxes in Fig. 5). Next,

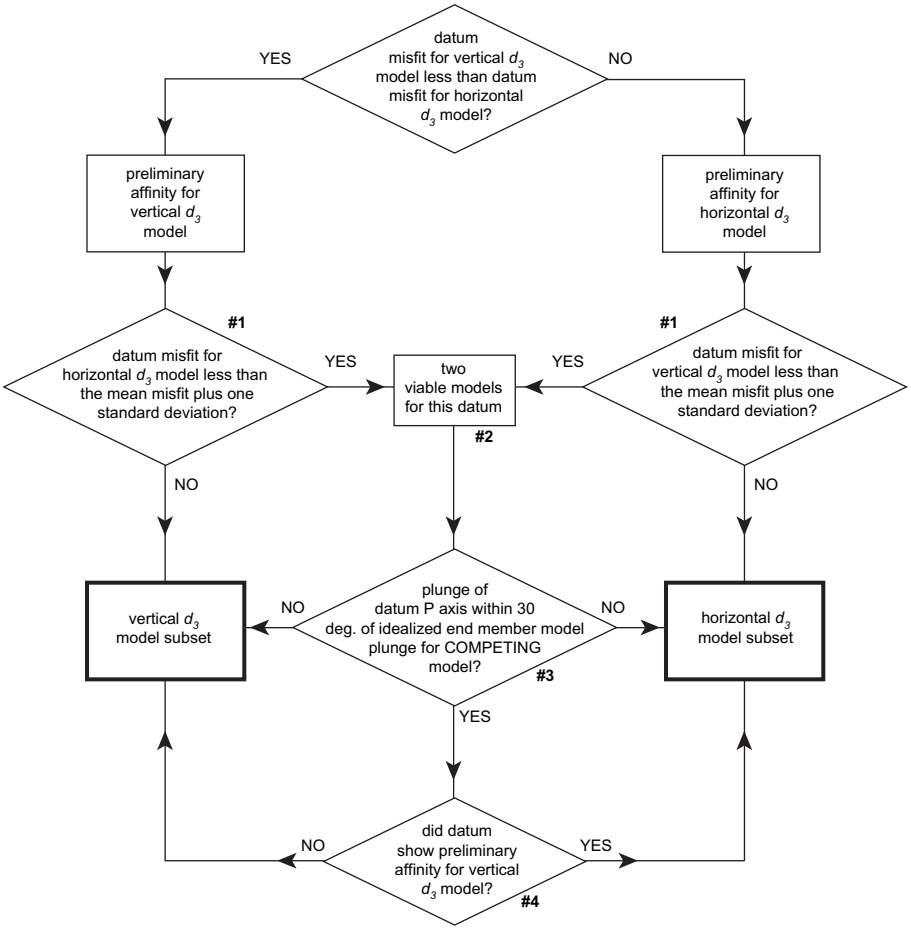

Fig. 5. Flow chart describing the approach used to subdivide data sets for which two nearly orthogonal solutions are suggested on the basis of preliminary inverse modeling. The numbers 1–4 are described in the text.

for each datum the viability of the *competing* model was determined by comparing its misfit with the mean misfit plus one standard deviation (see #1 in Fig. 5). This simple comparison identified data for which both initial models performed reasonably well (see #2 in Fig. 5).

To ensure consistency between the assigned data subset and the kinematics inferred on the basis of the focal mechanisms, the plunge of the P axis for each datum with two viable models was examined. If the plunge was within 30° of vertical for a datum initially assigned to the subhorizontal d_3 model subset, or within 30° of horizontal for a datum initially assigned to the subvertical d_3 model subset (see #3 in Fig. 5), the datum was reassigned (see #4 in Fig. 5). The choice of a 30° range for comparisons was designed to provide clear separation between data points that might justifiably be accounted for by both models from those that show a kinematic compatibility with just one model. At the same time, this choice limited the number of data points that moved from one model affinity to the other. In the case of the 205 events shown in Fig. 4 this approach yielded two strain-geometry subsets, one dominated by steep seismic P axes and one dominated by subhorizontal seismic P axes.

4.2.3. Magnitude-based subsets

To test whether the heterogeneity that is evident from the analysis of the subset of 205 events (Fig. 4) is related to earthquake size, the events were further grouped on the basis of magnitude. This analysis addresses potential magnitude dependence in the distribution of seismogenic strain. Three magnitude bins were defined, $M3.5-M3.9$ events ($3.5 \leq M \leq 3.9$), $M3.0-M3.4$ events ($3.0 \leq M \leq 3.4$), and $M2.5-M2.9$ events ($2.5 \leq M \leq 2.9$), containing 11, 30 and 160 events, respectively. The events in each grouping were analyzed for homogeneity and then (as appropriate) strain-geometry affinity (Fig. 5). Because there are only four events of $M \geq 4.0$, too few to invert for partial strain-rate tensors, a total of 201 events were examined using this approach.

The first test of homogeneity was an inversion of the magnitude-based subsets using 100 bootstrap data sets (see Section 2; Fig. 6). This is a computationally-efficient means of evaluating the potential for multiple solutions within a given magnitude range. Inhomogeneity is suggested for the 205, $M \geq 2.5$ events by the lack of systematic variation in the plunge of the seismic P axes with depth (Figs. 3c and 6a). The smallest magnitude subset, $M2.5-M2.9$ shows a weak girdle of seismic P axes akin to that for all 205 of the $M \geq 2.5$ events initially separated from the full data set (compare Figs. 3b and 6b, left). The bootstrap statistics likewise indicate two viable strain geometries on the basis of d_3 orientation (Fig. 6b, right), thus the individual events show an affinity for one of two possible strain geometries. The intermediate magnitude subset, $M3.0-M3.4$ displays a girdle of seismic P axes, however it is less prominent than for the smaller magnitude bin (Fig. 6c, left). The bootstrap statistics suggest a range of strain geometries with steep d_3 axes dominant and shallow south plunging d_3 axes subordinate (note the contour lines in Fig. 6c, right). Lastly, the larger magnitude subset, $M3.5-M3.9$ yields a single solution on the

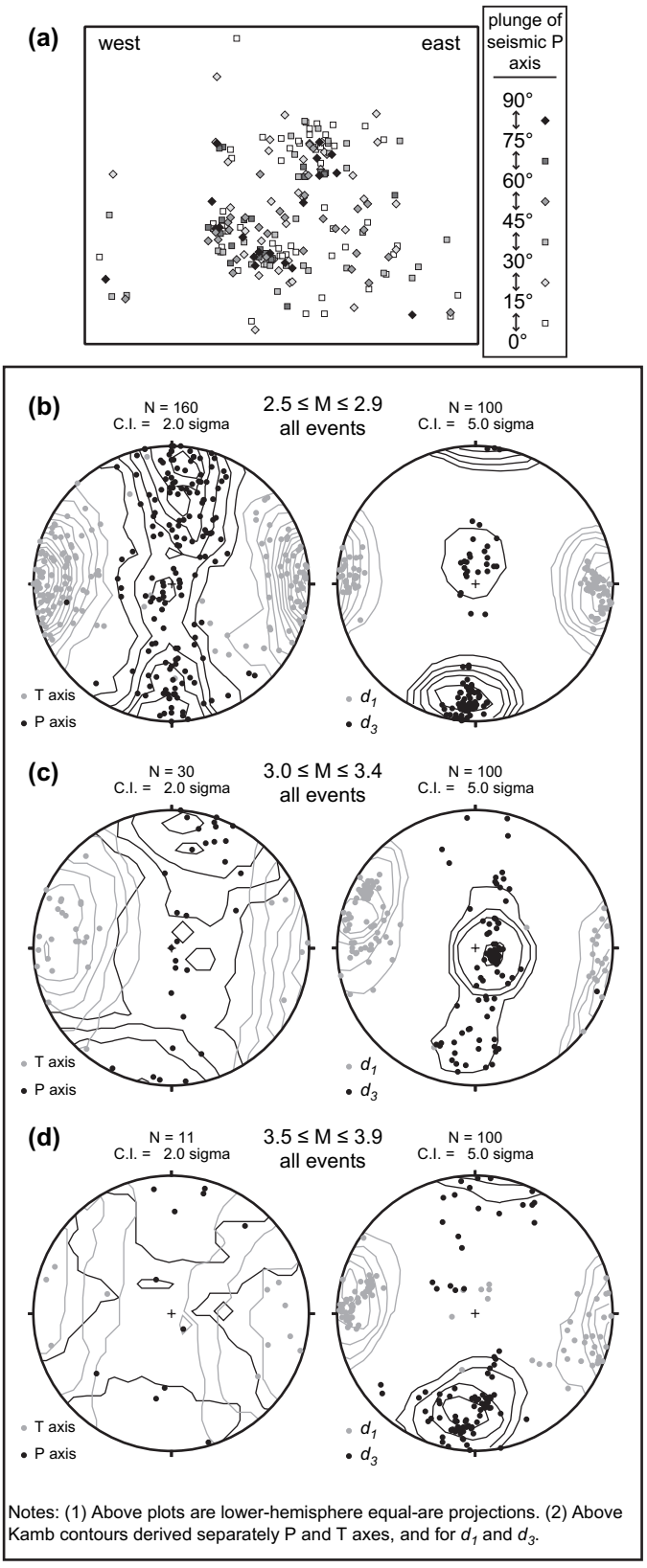

Fig. 6. Profile view of 201 western Indian Wells Valley earthquakes shaded to reflect the plunges of the seismic P axes (a), and summary of preliminary inversion results for these events in three subsets; (b) $M2.5-M2.9$ events, (c) $M3.0-M3.4$ events, and (d) $M3.5-M3.9$ events. (b)–(d) show seismic P and T axes on the left and the final positions of d_1 and d_3 for inversions of 100 bootstrap data sets on the right.

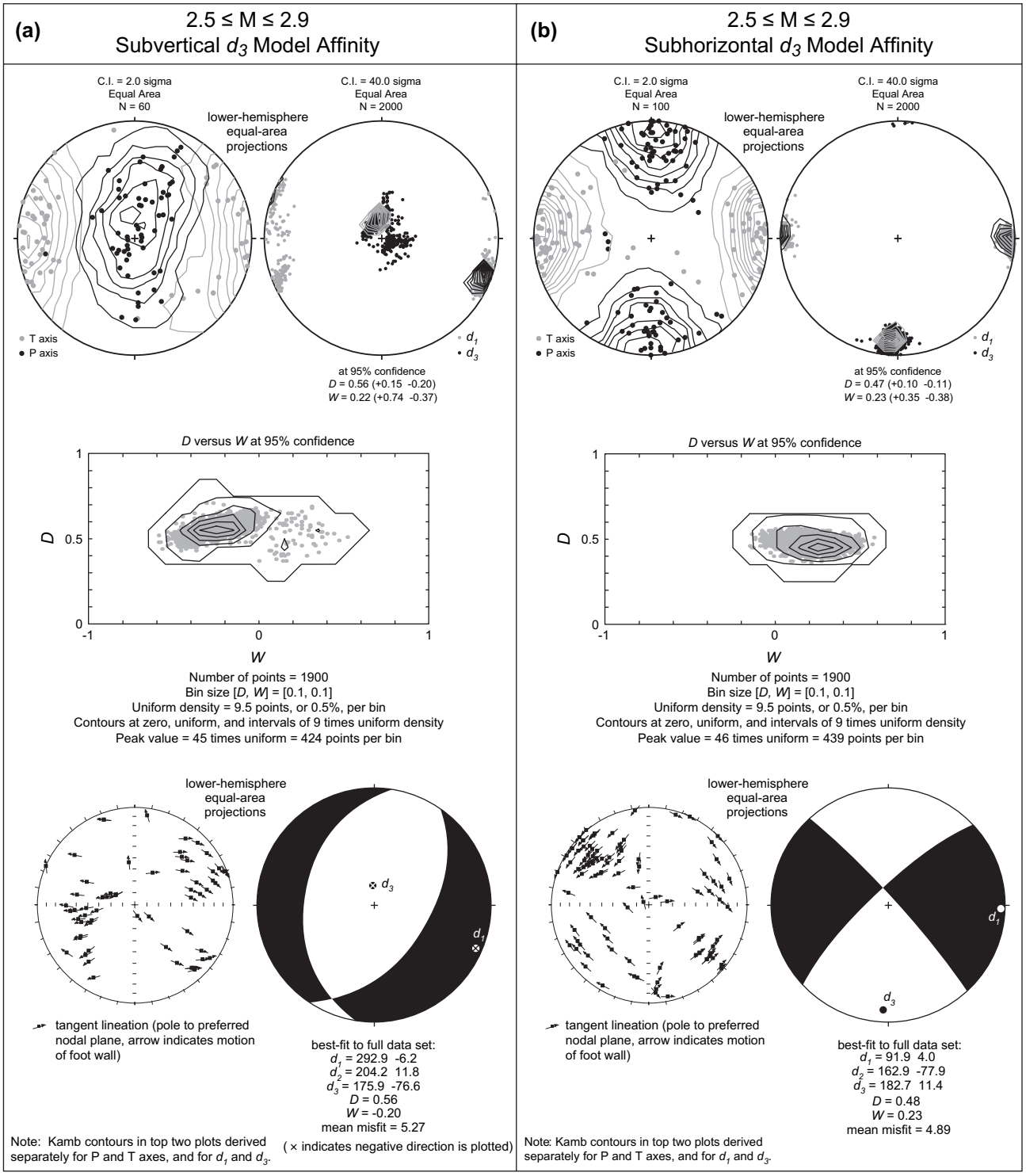

Fig. 7. Strain inversion results for the $M2.5-M2.9$ seismic events in the western Indian Wells Valley. The two subsets (a) and (b) were defined using the approach outlined in Fig. 5, and on the basis of the two maxima for d_3 axes in the preliminary inversions (Fig. 6a, bottom). (a) Events with an affinity for a strain geometry characterized by a subvertical d_3. (b) Events with an affinity for a strain geometry characterized by a subhorizontal d_3. (a, b) Consist of plot as follows: upper left, seismic P (black) and T (gray) axes; upper right, final positions of d_1 (gray) and d_3 (black) for inversions of 2000 bootstrap data sets, including statistical ranges for D and W at 95% confidence; middle, contoured dot plot of D versus W for the bootstrap data sets within 95% confidence limits ($N = 1900$); lower left, tangent lineation plot of preferred model nodal planes for the best-fitting model for the full data set (not for the bootstrap data sets); lower right, partial strain-rate tensor showing the positions of d_1 and d_3, with best-fitting model parameters at bottom. The boundary between black and white fields is the locus of points of zero stretching rate.

basis of the principal strain-rate axes for 100 bootstrap data sets (Fig. 6d).

Analysis of the $M2.5-M2.9$ subset as described in Fig. 5 reveals two viable seismogenic strain geometries. Inversion of 2000 bootstrap data sets for each subpopulation provides confidence limits that reveal how well the models describe the focal mechanism data. The final positions of both d_1 and d_3 for the 2000 bootstrap data sets for each subset are well clustered, and are in agreement with expectations on the basis of the kinematic axes (compare upper left and upper right plots in Fig. 7a,b). At 95% confidence, parameters D and W cannot be shown to be different than 0.5 and 0, respectively (upper right and middle Fig. 7a,b). Thus, the partial strain-rate tensors indicate plane strain and block rotation rates that are not significantly different than the rotation rates for the large-scale continuum. Both tensors are characterized by subhorizontal d_1 and either subvertical d_3 (Fig. 7a, bottom right) or subvertical d_2 (Fig. 7b, bottom right). The preferred model nodal planes for the two data subsets are dominantly distinct in orientation, although a few appear to be nearly identically oriented (Fig. 8).

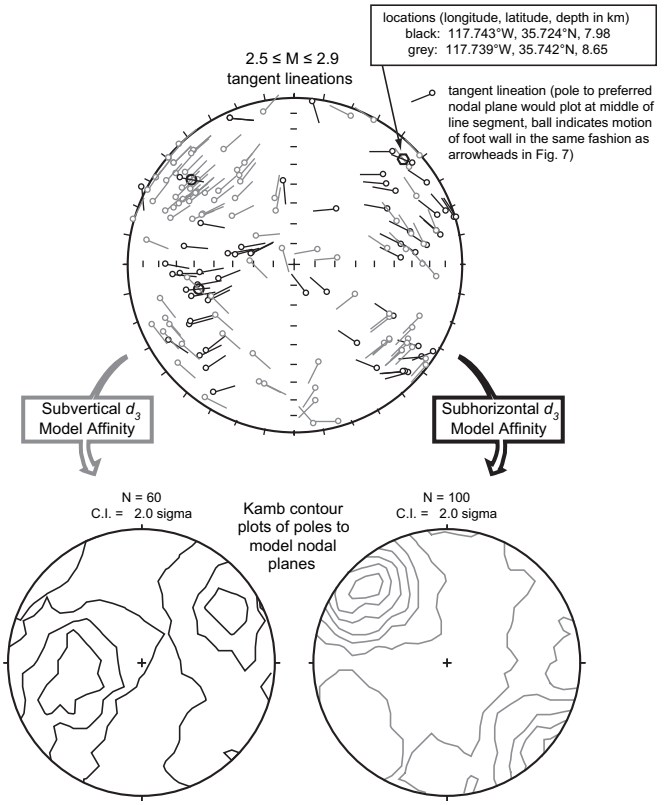

Fig. 8. Lower-hemisphere equal-area projection showing the tangent lineations of preferred model-nodal planes for the two data subsets from the $M2.5-M2.9$ events in western Indian Wells Valley. Black symbols = affinity for a model with subvertical d_3. Gray symbols = affinity for a model with subhorizontal d_3. Two similarly oriented nodal planes are indicated with circles. One pair of similarly oriented nodal planes that are ~1 km from one another is indicated with a polygon, and the coordinates for the two events are shown. The slip direction for the footwall is shown with a ball. Kamb contour plots for the preferred nodal planes are shown at the bottom left and bottom right, and are shaded as in the tangent lineation plot. See text for discussion.

The $M3.0-M3.4$ and $M3.5-M3.9$ bins contain fewer events, and as a consequence bootstrap statistics reveal considerably greater dispersion of model parameters than for the $M2.5-M2.9$ events (compare Figs. 7 and 9). Nonetheless, for the $M3.0-M3.4$ subset two partial strain-rate tensors can be resolved (Fig. 9a,b). These two strain geometries, and the relative number of events that define them, are nearly identical to those derived for the $M2.5-M2.9$ subset. That is, the majority of the events are characterized by subhorizontal d_1 and d_3, whereas the remainder are characterized by subhorizontal d_1 and d_2. In contrast, the $M3.5-M3.9$ events can be fit with a single partial strain-rate tensor (Fig. 9c) that has subhorizontal d_1 and d_3.

5. Discussion

Non-recoverable strain associated with background seismic events in the western Indian Wells Valley is partitioned at ~km scales. The relatively small location errors for these events, ~1 km horizontal and ~2 km vertical, have prevented further spatial separation into subsets of events with comparable focal mechanisms. These events, thus reflect strain within a single volume of crust, yet the diversity of focal mechanisms indicates that the strain is kinematically heterogeneous. Inverse modeling of focal mechanisms reveals that the events generally show an affinity for one of two partial strain-rate tensors with sub-perpendicular principal axes, and that deformation is thereby partitioned to structures that are spatially intermixed.

5.1. M2.5–M2.9 and M3.0–M3.4 subsets

The partial strain-rate tensors determined for $M2.5-M2.9$ and $M3.0-M3.4$ earthquake subsets are in accord with expectations from the preliminary inversion of 1000 bootstrap data sets (see Section 2) for pooled $M \geq 2.5$ background events (Fig. 4). In particular, the events show an affinity for solutions consistent with either crustal thinning or horizontal shearing. The earthquake hypocenters that define these two dominant strain geometries are spatially intermixed (Figs. 8 and 10). The best-fitting models for horizontal shearing in these two subsets are characterized by subhorizontal east-west trending d_1 and subhorizontal north-south trending d_3 (Figs. 7 and 9). The preferred model-nodal planes for the horizontal shearing solutions are mostly steeply southeast-dipping, however, subordinate numbers dip steeply west and northwest (Fig. 10b, inset in blue). The crustal thinning solutions are each characterized by subhorizontal west northwest-east southeast trending d_1 and subvertical d_3. Two orientations for the preferred model-nodal planes are apparent, moderate east dips are dominant and steep west southwest dips are subordinate (Fig. 10b, inset in orange).

In total, these results indicate that the 3D deformation that is accommodated by the $M2.5-M2.9$ and $M3.0-M3.4$ events can be explained by pairs of nearly orthogonal partial strain-rate tensors that swap d_2 and d_3 orientations with a generally constant d_1 geometry.

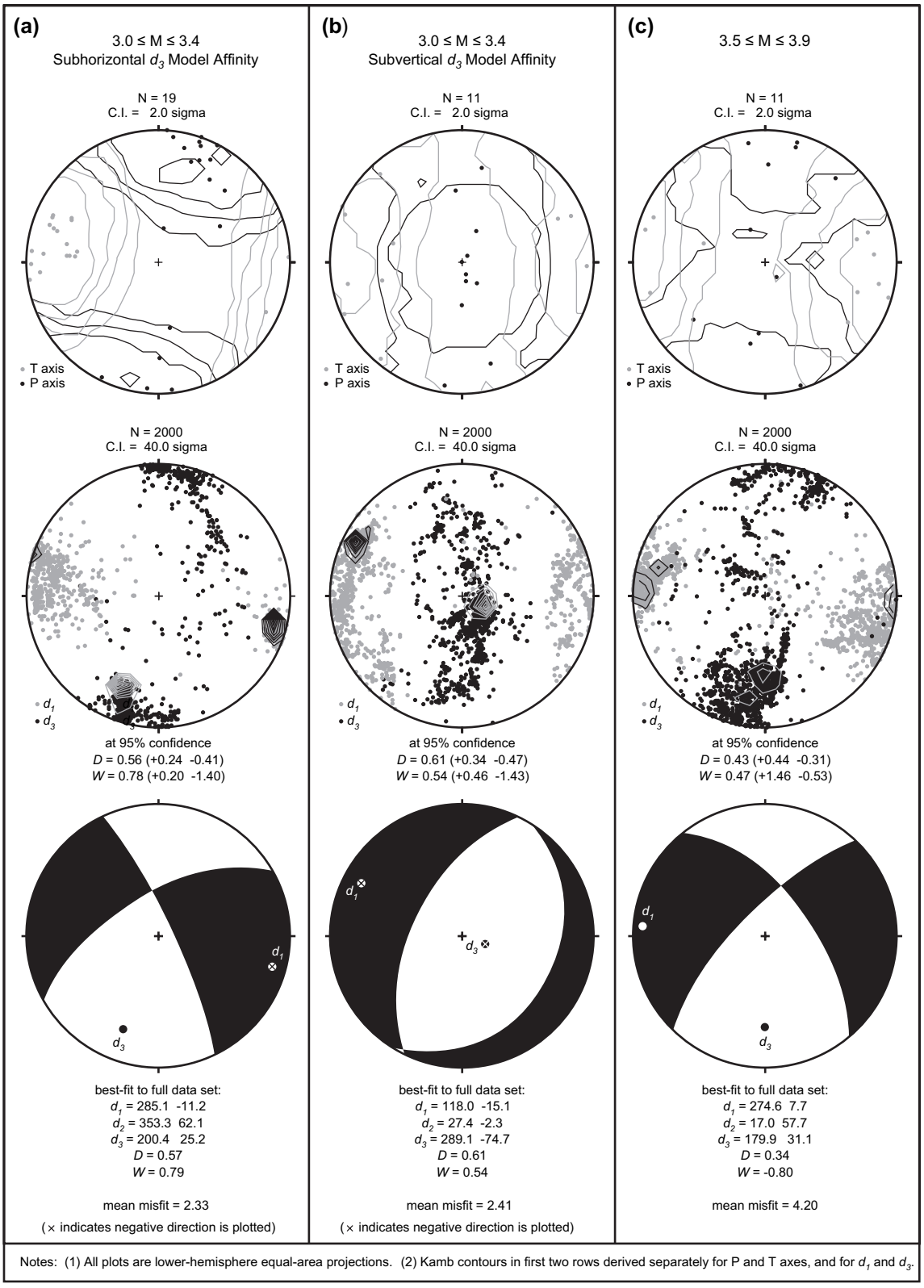

Fig. 9. Strain inversion results for the *M*3.0–*M*3.4 and *M*3.5–*M*3.9 seismic events in western Indian Wells Valley. (a, b) Show results for two strain-geometry subsets of *M*3.0–*M*3.4 events. (c) shows results for all of the events in the *M*3.5–*M*3.9 bin.

5.2. M3.5–M3.9 subset

The eleven events in the *M*3.5–*M*3.9 subset define a single partial strain-rate tensor consistent with horizontal shearing, much like those derived for the *M*2.5–*M*2.9 and *M*3.0–*M*3.4 events (compare Fig. 9c, bottom with 9a, bottom and 7b, lower right). The preferred model-nodal planes suggest that these larger events accommodate both right slip and left slip

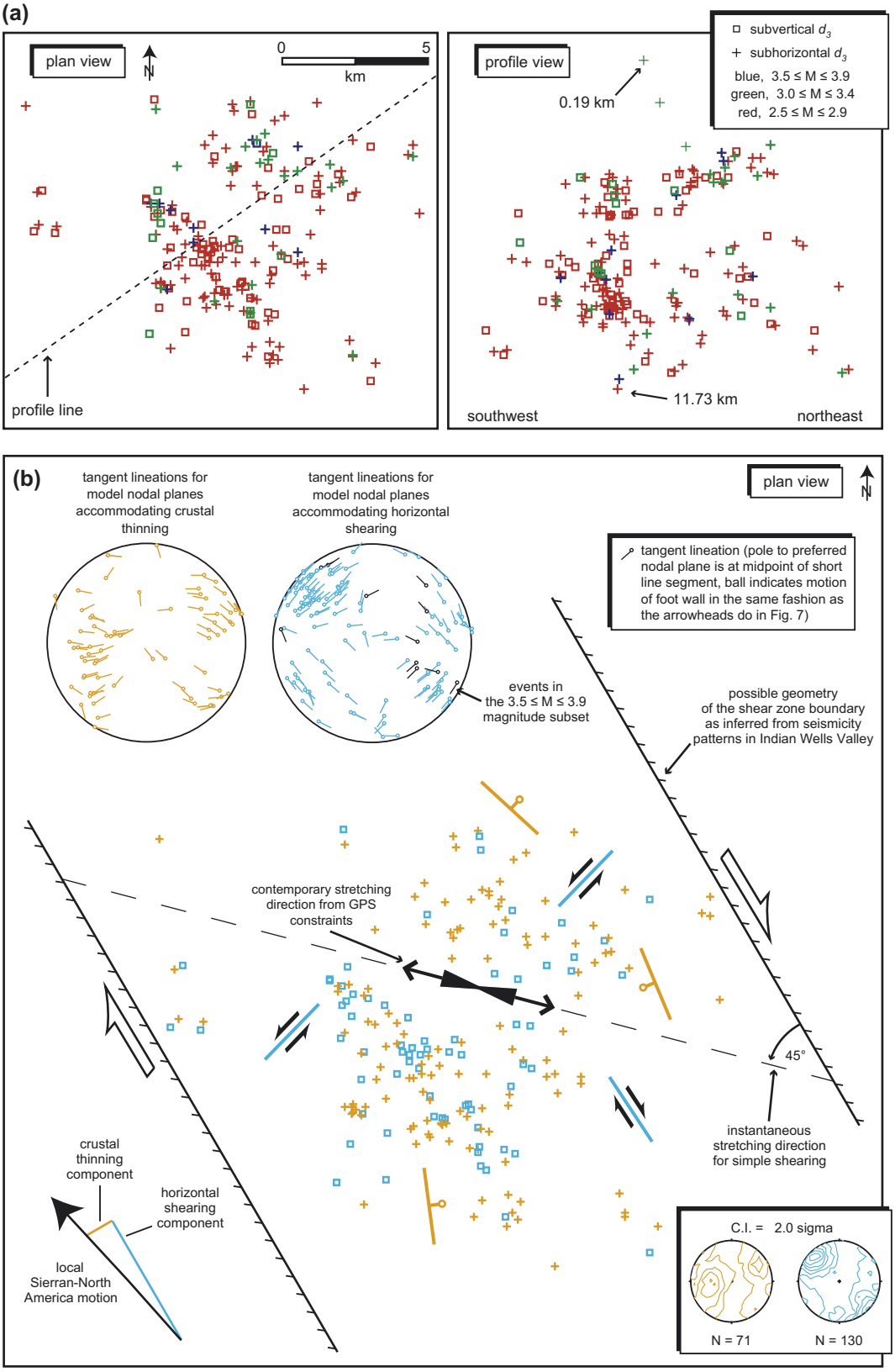

Fig. 10. (a). Plan and profile views of the seismic events in the three magnitude bins defined for the western Indian Wells Valley. Events with an affinity for a partial strain-rate tensor with subvertical d_3 are shown as open squares and events with an affinity for a partial strain tensor with subhorizontal d_3 are shown as plus signs. The magnitude bins are color coded (see key). See text for details. (b). Plan view conceptual model for the kinematics of western Indian Wells Valley. The seismic events are depicted with symbols as in (a), and color coded to reflect the strain geometry that the events accommodate (see Figs. 7–9). The preferred model nodal planes are shown in two lower-hemisphere equal-area projections. The pattern of seismicity in Indian Wells Valley is used to constrain the geometry for the shear zone boundary. Contemporary stretching from GPS geodesy is nearly parallel to the instantaneous stretching direction for simple shearing (see Fig. 1b). The local trajectory of Sierran-North America motion (Dixon et al., 2000) is shown with the large arrow at lower left. Inset at lower right shows Kamb contour plots for the model nodal planes shown at the top.

(Fig. 10b, black tangent lineations). This result indicates that strain partitioning is restricted to the smaller events (i.e., the $M2.5-M2.9$ and $M3.0-M3.5$ events).

5.3. Scale of strain partitioning

The 3D distribution of the modeled seismic events in the various subsets defined for western Indian Wells Valley is heterogeneous and no relations between depth or horizontal position and strain geometry are apparent. In plan and profile views the events in the subpopulations as defined by magnitude and strain geometry are spatially intermixed (Fig. 10a). In addition, the preferred model-nodal planes for the two strain geometries that best fit the $M2.5-M2.9$ events (160 events total) are largely distinct in orientation (Fig. 8) suggesting that different faults primarily accommodate different strain geometries. This is also true when considering the strain geometry affinities for the 201 pooled $M < 4$ events (Fig. 10b, inset).

Despite the foregoing observations, several examples of nearly identically-oriented preferred model-nodal planes appear to accommodate different strain geometries (circles, Fig. 8), and in one case the seismic events occur within ~1 km one another (polygon with coordinates, Fig. 8). These observations suggest the possibility that an individual fault plane might accommodate different strain geometries during different events. The relative proximity of these events is important in the context of interpreting multiply lineated faults in the rock record (Angelier, 1994; Lewis and Byrne, 2001). Moreover, the larger events ($M3.5-M3.9$) are characterized by rupture radii that are large enough, hundreds of meters, to facilitate interactions with other rupture surfaces. Such interactions would have important implications on the mechanics of the fault system, including influencing resolved incremental shear strains on fault surfaces (Twiss et al., 1993).

5.4. Boundary conditions

In the western Indian Wells Valley (Fig. 10b), non-recoverable strain is interpreted to reflect large-scale divergent strike-slip boundary conditions (Dixon et al., 1995, 2000; Unruh et al., 2002, 2003). The components of horizontal shearing and crustal thinning can be assessed by assuming that the shear-zone boundaries for the Airport Lake fault zone are constrained by the northwest-striking nodal plane of the 1995 Ridgecrest earthquake, and the associated earthquake swarm (Fig. 1). The small-circle motion of the Sierran microplate relative to North America is rotated counter clockwise from the shear zone boundaries, providing a component of extension across the zone.

The modeled partitioning of strain is consistent with expectations based on theoretical analyses of general strain. Assuming that work minimization controls the orientations of faults and that cohesion provides the resistance to fault slip, Reches (1978) showed that four or more sets of faults are required to accommodate a general 3D deformation. The subsets of seismic events defined on the basis of affinity for different partial strain-rate tensors (i.e., for two models with distinct d_3 orientations) are each characterized by at least two distinct orientations for preferred model nodal planes (Fig. 8, bottom; Fig. 10b, inset). The preferred model-nodal planes are selected from the two possible nodal planes for each datum on the basis of minimum misfit, and thus although their physical significance is unknown (Michael, 1987) it is expected that they reflect viable shear plane geometries.

Differences in the geometry of the regional-scale crustal boundaries appear to be reflected in the strain accommodated by background earthquakes, most notably in the scale over which strain is partitioned. As noted above, the seismic activity in western Indian Wells Valley occurs within a fault zone with a relatively small component of divergence (Fig. 10b). In contrast, the area of Wild Horse Mesa is more divergence-dominated (Fig. 2; Unruh et al., 2003). Wild Horse Mesa is situated at a right-releasing stepover in a dextral strike-slip fault system (Unruh et al., 2002, 2003). This stepover is marked by north-striking normal faults, the Coso volcanic and geothermal fields (Figs. 1 and 2), and has been identified as a nascent metamorphic core complex (Monastero et al., 2005). As a consequence, the contemporary stretching direction is at a much larger than 45° angle to the probable zone-bounding structures. The depth-dependent strain apparent in the seismogenic deformation at Wild Horse Mesa appears to reflect these factors, and is consistent with results of analog modeling of this structure by Dooley et al. (2003).

6. Conclusions

The results of this work: (1) provide clues about how the crust responds to divergent strike-slip motion during the relatively early stages of continental shearing; and (2) have implications for interpreting the rock record. The record of seismogenic deformation in the western Indian Wells Valley of eastern California suggests that large-scale triaxial deformation is partitioned at ~km scales to sets of normal and strike-slip faults. From this study the following conclusions are drawn:

1. The $M2.5-M2.9$ and $M3.0-M3.4$ earthquake subsets are best-fit by pairs of partial strain-rate tensors that reflect plane strain, and that are oriented nearly orthogonally with respect to one another (Fig. 7a,b. lower right, Fig. 9a,b). Each pair of tensors is characterized by subhorizontal east-west trending d_1 and one of the two is characterized by a subvertical d_3 whereas the other is characterized by a subvertical d_2.
2. The largest magnitude events analyzed in detail ($M3.5-M3.9$ events) are best fit by a single partial strain-rate tensor, consistent with horizontal shearing that includes a small component of crustal thinning (Fig. 9c). Strain partitioning, thus displays a degree of magnitude dependence (see #1 above). This observation is consistent with the fact that the small-circle motion of the Sierran microplate is only slightly more westerly than the inferred zone-bounding structures in the western Indian Wells Valley (Fig. 10b).
3. The seismic events defining these plane strains are intimately intermixed in space at ~km scales. These results indicate the accommodation of a triaxial large-scale deformation by a system of essentially coeval structures that

accommodate two homogeneous plane strains. This interpretation is in accord with theoretical modeling that indicates that at least four sets of faults are necessary to accommodate a 3D deformation.

4. The mismatch between Sierran-North America motion and the geometry of the Airport Lake fault zone results in divergent strike-slip motion that appears to be accommodated by partitioned strain reflected by the *M*2.5–*M*2.9 and *M*3.0–*M*3.4 earthquake subsets. The majority of the background seismic moment release is associated with horizontal displacement accommodated by conjugate strike-slip faulting (Figs. 7 and 9a,b). Less prevalent shear-zone-normal extension is accommodated by normal faulting.

Acknowledgments

This work was supported in part by an NSF Earth Science Postdoctoral Fellowship and by a contract with the U.S. Navy Geothermal Program Office (number N68936-01-C-0094). I thank R. Twiss, J. Unruh and F. Monastero for many fruitful discussions during the course of this work, and R. Twiss and M. Cooke for access to computing facilities at UC Davis and UMass, respectively. Digital versions of the focal mechanism catalog provided by E. Hauksson and of the GPS data provided by S. McClusky are much appreciated. Thanks to R. Twiss for the inversion programs FLTSLP and GPSTRN (for inverting GPS velocities) and to the following individuals for post-processing programs used in the analysis: R. Twiss for DWcontr and MPSOL; R. Allmendinger for Stereonet, S. Hurst for TanLin, and P. Wessel and W.H.F. Smith for GMT. The work of L. Guenther to automate the search procedure and include statistical capabilities in the program FLTSLP is very much appreciated. Finally, the critical comments of reviewers D. Harry and M. Markley, and editor W. Dunne served to substantially improve this paper.

Appendix A. Supplementary material

Supplementary material for this manuscript can be downloaded at doi:10.1016/j.jsg.2007.02.015.

References

Amelung, F., King, G., 1997. Large-scale tectonic deformation inferred from small earthquakes. Nature 386, 702.

Angelier, J., 1990. Inversion of field data in fault tectonics to obtain regional stress-III. A new rapid direct inversion method by analytical means. Geophysics Journal International 103, 363–376.

Angelier, J., 1994. Fault slip analysis and paleostress reconstruction. In: Hancock, P.L. (Ed.), Continental Deformation. Pergamon Press, Oxford, pp. 53–100.

Carey-Gailhardis, E., Mercier, J.L., 1992. Regional state of stress, fault kinematics and adjustments of blocks in a fractured body of rock: application to the microseismicity of the Rhine graben. Journal of Structural Geology 14, 1007–1017.

Cashman, P.H., Ellis, M.A., 1994. Fault interaction may generate multiple slip vectors on a single fault surface. Geology 22, 1123–1126.

Cashman, S., Kelsey, H.M., Erdman, C.F., Cutten, H.N.C., Berryman, K.R., 1992. Strain partitioning between structural domains in the forearc of the Hikurangi subduction zone, New Zealand. Tectonics 11, 242–257.

Clark, M.B., Fisher, D.M., 1995. Strain partitioning and crack-seal growth of chlorite-muscovite aggregates during progressive noncoaxial strain; an example from the slate belt of Taiwan. Journal of Structural Geology 17, 461–474.

Cowen, D.S., 1999. Do faults preserve a record of seismic slip? A field geologist's opinion. Journal of Structural Geology 21, 995–1001.

Dewey, J.F., 2002. Transtension in Arcs and Orogens. In: International Geology Review 44. V.H. Winston & Sons, Inc, Silver Spring, MD, pp. 402–439.

Dixon, T.H., Robaudo, S., Lee, J., Reheis, M.C., 1995. Constraints on present-day Basin and Range deformation from space geodesy. Tectonics 14, 755–772.

Dixon, T.H., Miller, M., Farina, F., Wang, H., Johnson, D., 2000. Present-day motion of the Sierra Nevada block and some tectonic implications for the Basin and Range province, North America Cordillera. Tectonics 19, 1–24.

Dokka, R.K., Travis, C.J., 1990. Late Cenozoic strike-slip faulting in the Mojave Desert, California. Tectonics 9, 311–340.

Dooley, T., McClay, K., 1997. Analog modeling of pull-apart basins. American Association of Petroleum Geologists Bulletin 81, 1804–1826.

Dooley, T., McClay, K., Monastero, F.C., 2003. Scaled Sandbox Modeling of Transtensional Pull-Apart Basins – Applications to the Coso Geothermal System, Eighth Annual Geothermal Program Office Technical Symposium, Davis California.

Duffield, W.A., Bacon, C.R., 1981. Geologic map of the Coso volcanic field and adjacent areas, Inyo County, California. In: United States Geological Survey Miscellaneous Investigation Series Map I-1200. United States Geological Survey, Reston, VA. 1 sheet.

Duffield, W.A., Bacon, C.R., Dalrymple, G.B., 1980. Late Cenozoic volcanism, geochronology, and structure of the Coso Range, Inyo County, California. Journal of Geophysical Research 85, 2381–2404.

Fitch, T.J., 1972. Plate convergence, transcurrent faults, and internal deformation adjacent to Southeast Asia and the Western Pacific. Journal of Geophysical Research 77, 4432–4460.

Gephart, J.W., 1990. Stress and the direction of slip on fault planes. Tectonics 9, 845–858.

Golombek, M.P., Brown, L.L., 1988. Clockwise rotation of the western Mojave Desert. Geology 16, 126–130.

Hauksson, E., 2000. Crustal structure and seismicity distribution adjacent to the Pacific and North America plate boundary in southern California. Journal of Geophysical Research 105, 13875–13903.

Hauksson, E., Hutton, K., Kanamori, H., Jones, L., Mori, J., Hough, S., Roquemore, G., 1995. Preliminary report on the 1995 ridgecrest earthquake sequence in Eastern California. Seismological Research Letters 66, 54–60.

Kostrov, V.V., 1974. Seismic moment and energy of earthquakes, and seismic flow of rock. Physics of the Solid Earth 1, 13–21.

Lees, J.M., 2002. Three-dimensional anatomy of a geothermal field, Coso, southeast-central California. In: Glazner, A.F., Walker, J.A., Bartley, J.M. (Eds.), Geologic Evolution of the Mojave Desert and Southwestern Basin and Range. Memoir 195. Geological Society of America, Boulder, Colorado, pp. 259–276.

Lewis, J.C., Byrne, T.B., 2001. Fault kinematics and past plate motions at a convergent plate boundary: tertiary Shimanto Belt, southwest Japan. Tectonics 20, 548–565.

Lewis, J.C., Pluhar, C.J., 2003a. Pliocene to Recent Kinematics of the Wild Horse Mesa and Coso Wash: An Integrated Study Using Micropolar Theory and Paleomagnetic Determinations to Examine Spatial and Temporal Variations in Strain: Final Technical Report prepared for the Geothermal Program Office, Naval Air Warfare, Center, China Lake, California.

Lewis, J.C., Pluhar, C.J., 2003b. What can we learn from small non-recoverable strains at plate boundaries? In: American Geophysical Union Annual Meeting. Eos, Transactions, AGU 84. American Geophysical Union, San Francisco, CA. F-1433.

Lewis, J.C., Unruh, J.R., Twiss, R.J., 2003. Seismogenic strain and motion of the Oregon coast block. Geology 31, 183–186.

McCaffrey, R., 1992. Oblique plate convergence, slip vectors, and forearc deformation. Journal of Geophysical Research 97, 8905–8915.

McClusky, S.C., Bjornstad, S.C., Hager, B.H., King, R.W., Meade, B.J., Miller, M.M., Monastero, F.C., Souter, B.J., 2001. Present day kinematics of the eastern California shear zone from a geodetically constrained block model. Geophysical Research Letters 28, 3369–3372.

Michael, A.J., 1987. Use of focal mechanisms to determine stress: a control study. Journal of Geophysical Research 92, 357–368.

Monastero, F.C., Walker, J.D., Katzenstein, A.M., Sabin, A.E., 2002. Neogene evolution of the Indian Wells Valley, east-central California. In: Glazner, A.F., Walker, J.D., Bartley, J.M. (Eds.), Geologic Evolution of the Central Mojave Desert and Southern Basin and Range. Memoir 195. Geological Society of America, Boulder, Colorado, pp. 199–228.

Monastero, F.C., Katzenstein, A.M., Miller, J.S., Unruh, J.R., Adams, M.C., Richards-Dinger, K., 2005. The Coso geothermal field: a nascent metamorphic core complex. Geological Society of America Bulletin 17, 1534–1553.

Peacock, D.C.P., Anderson, M.W., Morris, A., Randall, D.E., 1998. Evidence for the importance of 'small' faults on block rotations. Tectonophysics 299, 1–13.

Philpotts, A.R., 1964. Origin of pseudotachylites. American Journal of Science 262, 1008–1035.

Pluhar, C.J., Coe, R.S., Sampson, D.E., Glen, J.M.G., Monastero, F.C., Tanner, S.B., 2005. Lava fingerprinting using paleomagnetism and innovative X-ray fluorescence spectroscopy: a case study from the Coso volcanic field, California. In: Geochemistry Geophysics Geosystems 6. American Geophysical Union and the Geochemical Society.

Pluhar, C.J., Coe, R.S., Lewis, J.C., Monastero, F.C., Glen, J.M.G., 2006. Fault block kinematics at a releasing stepover of the Eastern California Shear Zone: partitioning of rotation style in and around the Coso geothermal area and nascent metamorphic core complex. Earth and Planetary Science Letters 250, 134–163.

Press, W.H., Flannery, B.P., Teukolksy, S.A., Vettering, W.T., 1989. Numerical Recipes, the Art of Scientific Computing (FORTRAN version). Cambridge University Press, New York.

Reches, Z.E., 1978. Analysis of faulting in three-dimensional strain field. Tectonophysics 47, 109–129.

Roquemore, G., 1980. Structure, tectonics and stress field of the Coso Range, Inyo County, California. Journal of Geophysical Research 85, 2434–2440.

Schermer, E.R., Luyendyk, B.P., Cisowski, S., 1996. Late Cenozoic structure and tectonics of the northern Mojave Desert. Tectonics 15, 905–932.

Sonder, L.J., Jones, C.H., Salyards, S.L., Murphy, K.M., 1994. Vertical axis rotations in the Las Vegas Valley Shear Zone, southern Nevada: paleomagnetic constraints on kinematics and dynamics of block rotations. Tectonics 13, 769–788.

Tchalenko, J.S., 1968. The evolution of kink-bands and the development of compression textures in sheared clays. Tectonophysics 6, 159–174.

Twiss, R.J., Gefell, M.J., 1990. Curved slickenfibers: a new brittle shear sense indicator with application to a sheared serpentinite. Journal of Structural Geology 12, 471–481.

Twiss, R.J., Unruh, J.R., 1998. Analysis of fault slip inversions: do they constrain stress or strain rate? Journal of Geophysical Research 103, 12,205–12,222.

Twiss, R.J., Unruh, J.R. (in press). Structure, deformation, and strength of the Loma Prieta Fault, northen California, USA, as inferred from 1989–1990 Loma Prieta aftershock sequence, *Geological Society of America Bulletin*.

Twiss, R.J., Protzman, G.M., Hurst, S.D., 1991. Theory of slickenline patterns based on the velocity gradient tensor and microrotation. Tectonophysics 186, 215–239.

Twiss, R.J., Souter, B.J., Unruh, J.R., 1993. The effect of block rotations on the global seismic moment tensor and the pattern of P and T axes. Journal of Geophysical Research 98, 645–674.

Unruh, J.R., Lettis, W.R., 1998. Kinematics of transpressional deformation in the eastern San Francisco Bay region, California. Geology 26, 19–22.

Unruh, J.R., Twiss, R.J., 1998. Coseismic growth of basement-involved anticlines: the Northridge-Laramide connection. Geology 26, 335–338.

Unruh, J.R., Twiss, R.J., Hauksson, E., 1996. Seismogenic deformation field in the Mojave block and implications for tectonics of the eastern California shear zone. Journal of Geophysical Research 101, 8335–8361.

Unruh, J.R., Hauksson, E., Monastero, F.C., Twiss, R.J., Lewis, J.C., 2002. Seismotectonics of the Coso range-Indian Wells Valley region, California: transtensional deformation along the southeastern margin of the Sierra Nevada microplate. In: Glazner, A.F., Walker, J.D., Bartley, J.M. (Eds.), Geologic Evolution of the Central Mojave Desert and Southern Basin and Range. Memoir 195. Geological Society of America, Boulder, Colorado, pp. 277–294.

Unruh, J., Humphrey, J., Barron, A., 2003. Transtensional model for the Sierra Nevada frontal fault system, eastern California. Geology 31, 327–330.

Walker, J.D., Whitmarsh, R.S., 1998. A tectonic model for the Coso geothermal area. In: U.S. Department of Energy Proceedings Geothermal Program Review XVI, Berkeley, CA. pp. 2-17–2-24.

Wells, R.E., 1990. Paleomagnetic rotations and the Cenozoic tectonics of the Cascade arc, Washington, Oregon and California. Journal of Geophysical Research 95, 19409–19417.

Wells, R.E., Coe, R.S., 1985. Paleomagnetism and geology of Eocene volcanic rocks of Southwest Washington, implications for mechanisms of tectonic rotation. Journal of Geophysical Research 90, 1925–1947.

Wernicke, B., Snow, K.J., 1998. Cenozoic tectonism in the central basin and range: motion of the Sierran-Great Valley block. In: Ernst, W.G., Nelson, C.A. (Eds.), Integrated Earth and Environmental Evolution of the Southwestern United States; the Clarence A. Hall, Jr. volume. Bellwether Publishing, Columbia, MD, pp. 111–118.